

Cross-Slot Metal-Mesh Bandpass Filters for Far-Infrared Astronomy

Joanna Perido^a, Kevin Denis^b, Jason Glenn^b, Nicholas F. Cothard^b, Manuel Quijada^b, Jessica Patel^b, Edward Wollack^b, Tilak Hewagama^b, Shahid Aslam^b, and Peter K. Day^c

^aUniversity of Colorado Boulder
^bNASA Goddard Space Flight Center
^cJet Propulsion Laboratory

ABSTRACT

The far-infrared (IR) region is rich with information needed to characterize interstellar dust and to investigate the cold outer planets of the solar system and their icy moons. The proposed sub-orbital observatory the Balloon Experiment for Galactic INfrared Science (BEGINS) will utilize cryogenic instruments to map spectral energy distributions (SEDs) of interstellar dust in the Cygnus molecular cloud complex. A future high priority flagship mission Uranus Orbiter and Probe carrying a net flux radiometer (NFR) will study the in situ heat flux of the icy giants atmosphere to 10 bar pressure. These instruments require far-IR filters to define the instrument spectral bandwidths. Our ultimate goal is to define the instrument bands of BEGINS and the NFR with linear-variable filters (LVFs) and discrete-variable filters (DVs). The LVFs and DVFs will be made of metal mesh band-pass filters (MMBF) comprised of a 100 nm thick gold film with cross-shaped slots of varying sizes along a silicon (Si) substrate with cyclic olefin copolymer (COC) anti-reflection (AR) coatings. We present our progress towards LVFs and DVFs with simulated and measured transmission of a room temperature, non-AR coated, single-band 44 μm MMBF filter. We have successfully fabricated, measured, and modeled a non-AR coated, room temperature 44 μm MMBF. The transmission at room temperature and non-AR coated was measured to be 27% with a resolving power of 11. When COC-AR coated on both sides the transmission is expected to increase to 69% with a resolving power of 10.

Keywords: Infrared, filters, metal mesh, bandpass, astronomy, planetary sciences

1. INTRODUCTION

Observations of far-IR spectra are a necessary means to characterize interstellar dust that plays an important role in understanding galaxy evolution and star formation. The proposed sub-orbital observatory the Balloon Experiment for Galactic INfrared Science (BEGINS)¹ will utilize cryogenic instruments to map spectral energy distributions (SEDs) of interstellar dust in the Cygnus molecular cloud complex with a resolving power ($R = \lambda/\Delta\lambda$) of ~ 7 from 25-65 μm and of 3-6 from 70-250 μm . The far-IR region also provides astronomers with knowledge of planets' atmospheres and evolution. The future high priority flagship mission Uranus Orbiter and Probe will carry a net flux radiometer (NFR) to study the in situ heat flux of the icy giants atmosphere to 10 bar pressure.^{2,3} The NFR will measure Uranus's net radiation flux in seven spectral bands, spanning solar to infrared wavelengths (0.2 to 300 μm).³ Our ultimate goal is to define the instrument bands of BEGINS and the NFR with linear-variable filters (LVFs) and discrete-variable filters (DVs).

The LVFs and DVFs will be made of metal mesh band-pass filters (MMBF). MMBFs are frequency selective surfaces. Our MMBFs are comprised of metal thin-films with arrays of cross-slots (Fig. 1). MMBFs can be free-standing or deposited on a substrate. Our MMBFs are lithographically patterned on a silicon (Si) substrate. Research on MMBFs was first published by Ulrich in 1966⁴ for far-IR wavelengths and have since been

Further author information: (Send correspondence to Joanna Perido)
Joanna Perido: E-mail: joanna.perido@colorado.edu
Jason Glenn: E-mail: jason.glenn@nasa.gov

investigated for far-IR astronomy because they are compact, present an easy fabrication process, their response can be tailored by changing the cross-slot parameters, and they can be cooled to liquid helium temperatures.⁵⁻⁹

Here, we present our work on a 44 μm MMBF. This is preliminary work towards LVFs and DVFs for both BEGINS and the NFR. The filter is made of 100 nm thick gold and will be supported by a silicon (Si) substrate. Gold was chosen as the thin-film because of its low resistivity which allows for high transmission. By making it 100 nm thick it is ~ 5 times larger than the skin depth of gold at the desired bandpass frequency. We use high-resistivity floatzone Si wafers for low loss. In this paper, we present simulations to predict the transmission profile of the 44 μm MMBF with a specific cross-slot size. The simulations are compared to measurements of the fabricated filters. We also present and discuss a transmission-line model to model the transmittance of the MMBF.

The paper is organized as follows: Section 2, discusses the 44 μm MMBF design, Section 3, discusses two model methods, simulations (3.1) and a transmission-line model (3.2). Section 4, describes the filter fabrication process. In Section 5, we discuss the filter measurements and compare the measurements to the models. In the last section, Section 6, we add concluding remarks and discuss future work on filters for BEGINS and the NFR.

2. FILTER CROSS-SLOT DESIGN

The transmission profile of a MMBF is determined by its cross-slot parameters; the periodicity (G), the cross-length (K) and the cross-width (B),⁵⁻⁹ Fig. 1. The bandpass center peak scales with K and the bandwidth becomes small as the ratios of G/K and G/B increase.⁶ The cross-slot parameters for the 44 μm MMBF were first estimated from conversion factors for λ_0 to the cross-length and periodicity, found in Melo, et al.⁸ λ_0 , will change in the Si medium so it must be divided by the refractive index of Si ($n_{Si} = 3.42$) before applying the conversion factors. The estimated parameters were then optimized through the use of simulations to achieve the desired bandpass peak. These simulations are discussed in section 3.1. The simulation optimized cross-slot parameters are shown in Table 1 and were used for fabrication of the 44 μm MMBF.

Table 1. 44 μm MMBF design cross-slot parameters G , K , and B (Fig. 1).

Parameter	(μm)
G	11.4
K	7.5
B	1.0

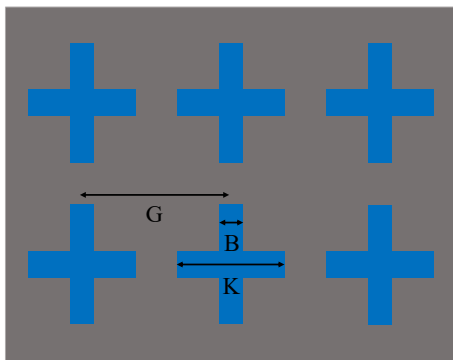


Figure 1. Illustration of metal-mesh cross-slot parameters. G is the periodicity, K is the cross-length and B is the cross-width. Gray represents gold film. Blue represents bare Si substrate.

3. FILTER MODELING

3.1 Simulations

In order to predict and model the MMBF performance we used Ansys High Frequency Structure Simulator (HFSS)* simulations. HFSS, a full-wave frequency domain electromagnetic field solver based on the finite element method, numerically solves Maxwell's equations across a specified frequency range for a specified structure geometry, material configuration, and boundary conditions. Through symmetry, an array of cross apertures in 100 nm gold on a Si substrate can be simulated by a single unit cell with perfect electric (\vec{E}) and magnetic (\vec{H}) field boundary conditions.^{6,9} The unit cell structure is shown in Fig. 2 *Left*. The perfect \vec{E} and \vec{H} field boundary conditions are applied to the side walls of the vacuum and Si boxes. Two wave ports are used at the top of the first vacuum box and at the bottom of the second vacuum box to simulate an incident plane wave and calculate S-parameters. To reduce the simulation time, we only used a quarter of the structure shown in Fig. 2 *Left*, as seen in Fig. 2 *Right*. The gold was modeled as a 100 nm thick volume with a room temperature bulk conductivity of 3.33×10^7 Siemens/m. The conductivity was calculated from room temperature DC resistivity measurements of the gold film, equal to $0.3 \Omega/\text{sq}$. The Si was defined as a $537 \mu\text{m}$ thick volume with a relative dielectric permittivity, $\epsilon_r = 11.7$. Dielectric loss is not included in the simulations presented because we are using high-resistivity floatzone Si. The dielectric loss tangent was measured to be $\sim 1 \times 10^{-7}$, and through simulation we confirmed that this loss does not effect the transmission.

There is ~ 0.7 power loss at each vacuum-Si interface. Therefore, the filters on the instruments will be at cryogenic temperatures and have anti-reflection (AR) coatings. We expect this to increase the transmission because the conductivity of gold will increase at cryogenic temperatures and vacuum-to-Si reflective losses will decrease with AR coatings. To determine the increase in transmission we ran simulations of the structure shown in Fig. 2 *Right*. The cryogenic bulk conductivity is 1.33×10^8 Siemens/m. This was calculated from the DC residual-resistance ratio (RRR) of the gold film, measured to be 4.0. The reflective losses at the vacuum-to-Si interfaces are reduced with $\lambda_0/4$ thick cyclic olefin copolymer¹⁰ (COC) AR coatings. COC has a low index of refraction (~ 1.5) that will provide low reflective loss over a modest bandwidth at the vacuum-to-Si interfaces. In the simulation, the COC-AR coatings are defined as $\lambda_0/4$ thick volumes with a relative dielectric permittivity of 2.37.¹⁰ From the simulation we found that the addition of the AR coatings causes the original bandpass peak to shift to longer wavelengths by $\sim 0.6 \mu\text{m}$ because of a change in the effective capacitance of the MMBF. This shift was taken into consideration when choosing the cross-slot parameters in Table 1. The simulations are compared to measurements in section 5.1.

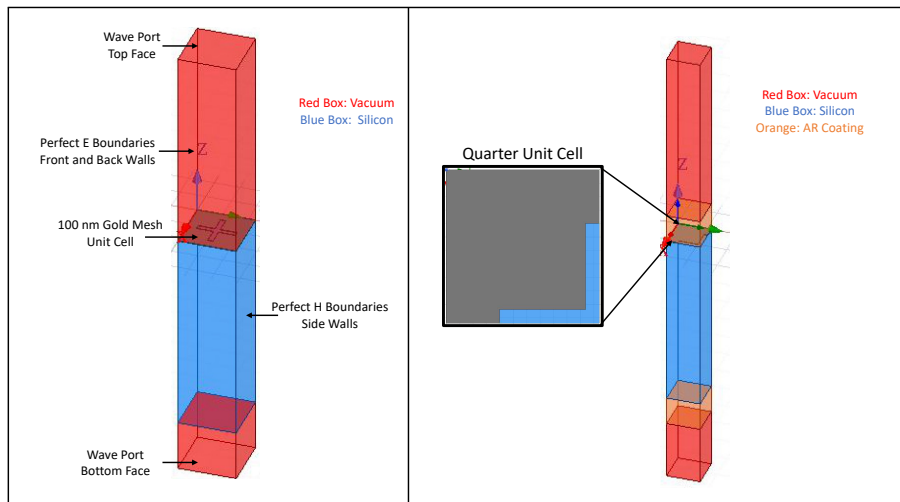


Figure 2. *Left*) 3D model of an HFSS unit cell simulation for a non-AR coated MMBF. *Right*) 3D model of an HFSS unit cell simulation for a double sided COC-AR coated MMBF. The quarter unit cell is used to reduce the simulation time. For illustration purposes, the vacuum, Si substrate and COC box heights are not to scale.

*<https://www.ansys.com/products/electronics/ansys-hfss>

3.2 Transmission-Line Model

The metal mesh cross-slots are self-resonant structures with an impedance that can be modeled as a passive LRC circuit.^{6,11,12} The reactive part of the LRC circuit determines the shape of the bandpass. The real part, while still contributing to the bandwidth, mainly represents the losses in the circuit. These are due to ohmic losses and dielectric losses in the Si medium. However, since the dielectric loss is small it is not added to the current model. The transmittance of our filters can then be modeled by placing the LRC circuit in a transmission-line model, as shown in Fig. 3. Where, $Z_0 = 377 \Omega/\text{sq}$, is the characteristic impedance of free-space. The Si is modeled as a transmission-line with length equal to thickness of the Si substrate ($537 \mu\text{m}$) with characteristic impedance, $Z_{\text{Si}} = Z_0/\sqrt{\epsilon_r} = 110 \Omega/\text{sq}$. This model is based on the transmission-line model used by Al-Azzawi, et al.¹² The impedance of this LRC circuit, Z_{LRC} , is

$$Z_{\text{LRC}} = \frac{R + j\omega L}{1 + j\omega RC - (\omega/\omega_0)^2}. \quad (1)$$

R is the resistance, C is the capacitance, L is the inductance, ω is the angular frequency and ω_0 is the circuit resonant angular frequency. In order to calculate the transmittance, the reflection coefficient, Γ , must be derived first. This is done by first calculating the load impedance, Z_{load} .

$$Z_{\text{Load}} = Z_{\text{Si}} \frac{Z_0 + jZ_{\text{Si}} \tan(\beta l_{\text{Si}})}{Z_{\text{Si}} + jZ_0 \tan(\beta l_{\text{Si}})} \quad (2)$$

where l_{Si} is the Si thickness ($537 \mu\text{m}$) and $\beta = \frac{2\pi}{\lambda_{\text{Si}}}$ is the wave-number. $\lambda_{\text{Si}} = \frac{\lambda}{n_{\text{Si}}}$, is the wavelength in the Si medium. Next, the equivalent impedance of the LRC circuit (Z_{LRC}) and load impedance must be calculated by adding them in parallel.

$$Z_{\text{eq}} = \frac{Z_{\text{Load}} * Z_{\text{LRC}}}{Z_{\text{Load}} + Z_{\text{LRC}}} \quad (3)$$

This allows us to derive the reflection coefficient,

$$\Gamma = \frac{Z_{\text{eq}} - Z_0}{Z_{\text{eq}} + Z_0} \quad (4)$$

The transmittance, which is equal to the fraction of incident power transmitted, is evaluated following Porterfield⁶ via, $T = 1 - |\Gamma|^2$. This model is fit to the HFSS simulated transmission of the MMBF to estimate L and C of the filter. We then compare the fit to both the simulations and the measurements in section 5.2.

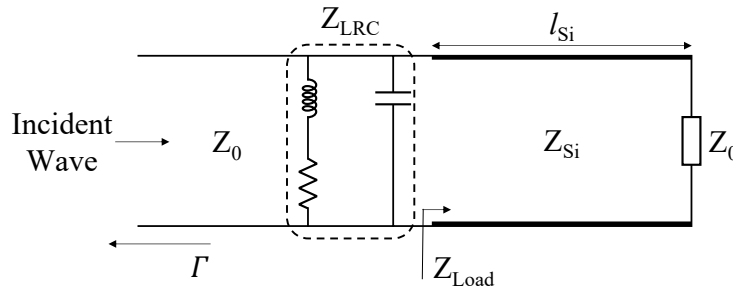


Figure 3. Transmission-line model representation of a MMBF on a Si dielectric. Z_0 , is the impedance of free-space, Z_{LRC} is the impedance of the MMBF, Z_{Si} is the impedance of Si, Z_{Load} is the load impedance at the beginning of the Si transmission line of length, l_{Si} . Γ , is the reflection coefficient used to calculate the fraction of incident power transmitted from the incident wave.

4. FABRICATION

The 44 μm MMBF was fabricated in a simple single layer process. Double side polished intrinsic float zone silicon wafers ($\rho > 20 \text{ k}\Omega\text{-cm}$) were coated with a 5 nm Ti adhesion layer and 100 nm thick Au layer by electron beam evaporation in the GSFC Detector Development Laboratory (DDL). The 44 μm MMBF has minimum features of 1 μm which were lithographically patterned by a Heidelberg DWL 66+ direct write laser system and a single layer of S1805 resist. The gold was etched by argon ion milling (4-Wave) and the titanium was further etched by a combination of fluorine plasma and hydrofluoric acid. Finally, the photoresist was removed by oxygen plasma and solvent cleaning. The filters were then diced into 25.4 mm by 25.4 mm squares for measurement. A scanning electron microscope image of the fabricated filter is shown in Fig. 4. The close up of one of the cross-slots shows the fabricated filter has rounded inner and outer edges, measured to have a radius of curvature of $\sim 0.5 \mu\text{m}$. The affects of the rounded corners were investigated through simulations and are discussed in the following section.

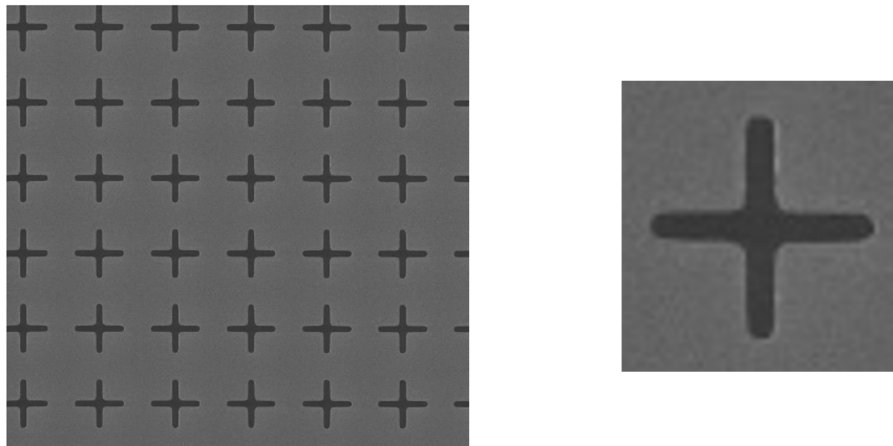


Figure 4. Scanning electron microscope (SEM) image of the fabricated 44 μm MMBF with cross-slot parameters presented in Table 1. The light gray is gold metal film and the dark gray is bare Si. The fabricated MMBF filter has rounded inner and outer edges with radius of curvature $\sim 0.5 \mu\text{m}$.

5. FTS TRANSMISSION MEASUREMENTS AND MODELING DISCUSSION

The transmission spectra of the 44 μm MMBF was measured using a Bruker IFS Fourier transform spectrometer (FTS) with a liquid-helium cooled bolometer. The data was collected over a spectral range from 76-650 cm^{-1} (15-132 μm) with a resolution of 1 cm^{-1} . The measured prototype 44 μm MMBF was non-AR coated and measured at room temperature. Deployed filters will be AR-coated and operated cryogenically. We did not have measurements of AR-coated filters at cryogenic temperatures ready for these *Proceedings*, but we are currently working on them. Here, we present HFSS simulations and preliminary measurements of the 44 μm MMBF.

5.1 44 μm MMBF Measurements vs Simulations

Fig. 5 shows the transmission spectra of the FTS measurement (blue dots) compared to the HFSS simulated transmission of the MMBF design cross-slot parameters (Design Parameters Sim, red solid curve). The fringing along the transmission profile is due to the Si cavity created between the metal mesh and the vacuum interface on the opposite side. The FTS resolution was small enough to barely resolve the fringes. In order for the simulations to match this, they were smoothed using a Gaussian filter to approximate the FTS apodization and resolution. The 44 μm MMBF was designed to have a band-pass peak at 7 THz with resolving power ~ 9 . However the measured filter has a bandpass peak at a slightly higher frequency, 7.1 THz, with a higher resolving power (~ 11) (Table 2). We determined this was due to differences in the designed MMBF's cross parameters and the fabricated cross parameters. Fig. 4 shows that the fabricated 44 μm MMBF is rounded at the inner and outer edges. The inside and outside edges of the cross are rounded to about 0.5 μm or half of the cross-width. Fig. 5 shows the change in the simulated filter transmission when the inner edges are rounded (HFSS Sim 1,

green solid curve), when the outer edges are rounded (HFSS Sim 2, yellow solid curve), and when both inner and outer edges are rounded (HFSS Sim 3, black solid line). When the the inner edges are rounded there is an increase in transmission because the area of the slot increases. There is also a slight shift in the bandpass peak to higher frequency, by 0.1 THz. For a cross-slot with only rounded outer edges, the transmission decreases due to a decrease in the slot area with a shift to higher frequency as well but it still does not match the measured bandpass peak. The peak shifts to higher frequencies because the rounding of the edges decreases the capacitance. When both the inner and outer edges are rounded the simulated transmission aligns better with the FTS measurement. The band-pass peak is at 7.1 THz, with a transmission of 26% and resolving power of ~ 11 . These simulations show how the filter's response is sensitive to changes in the cross-slot features and incorporating them allows us to model our measurements more accurately.

Fig. 6 shows the simulated transmission of a COC-AR coated, cryogenically cooled MMBF with the cross-slot unit cell used in HFSS Sim 3. The transmission increases by a factor of 2.63 to 69%, due to decreased gold resistive losses at cryogenic temperatures and decreased Si reflective losses from the addition of AR coatings. This is the expected transmission of our filters in an instrument.

Table 2. The bandpass peak, resolving power, and transmission of the simulated design parameters and FTS measured performances shown in Fig. 5 Left of the 44 μm MMBF.

	Design Parameters HFSS Sim	FTS Measurements
Band-pass Peak (THz)	6.9 (43 μm)	7.1 (42 μm)
$\lambda/\Delta\lambda$	9	11
Peak Transmission (%)	27	27

Simulated Quarter Cross-Slot Unit Cells

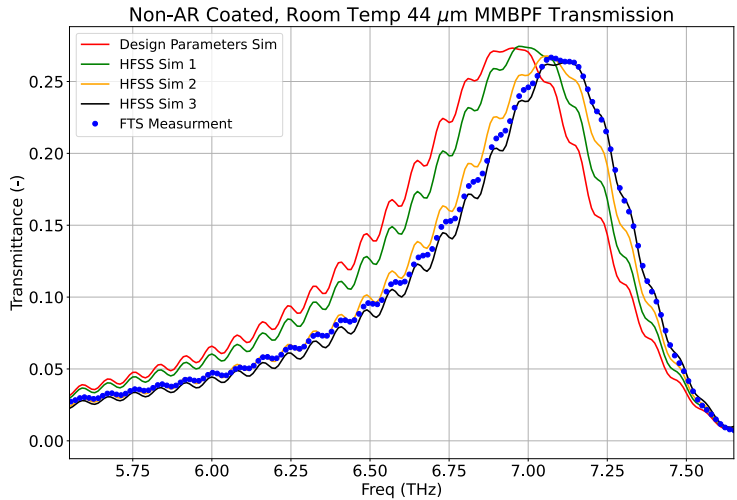
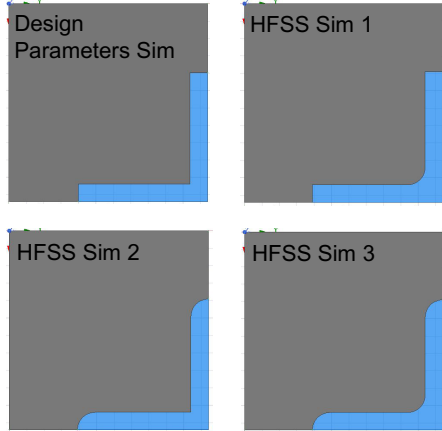


Figure 5. Left) The HFSS simulated quarter cross-slot unit cells of the simulated transmission shown in Fig. 5 Right for Design Parameters Sim, HFSS Sim 1, HFSS Sim 2, and HFSS Sim 3. Right) HFSS simulated and FTS measured transmittance of the non-AR coated, room temperature 44 μm MMBF. Red Line: HFSS unit cell with cross-slot parameters in Table 1. Green Line: HFSS Sim 1 has rounded inner corners (radius of curvature = 0.5 μm) with parameters: $G = 11.4 \mu\text{m}$, $B = 1 \mu\text{m}$, $K = 7.5 \mu\text{m}$. Orange Line: HFSS Sim 2 has rounded cross-ends (radius of curvature = 0.5 μm) with parameters: $G = 11.4 \mu\text{m}$, $B = 1 \mu\text{m}$, $K = 7.5 \mu\text{m}$. Black Line: HFSS Sim 3 has rounded cross-ends and inner corners (radius of curvature = 0.5 μm) with parameters: $G = 11.4 \mu\text{m}$, $B = 1 \mu\text{m}$, $K = 7.5 \mu\text{m}$. Blue: FTS measured transmission of fabricated 44 μm MMBF. The fringing along the transmission profile is due to the Si cavity created between the metal mesh and the vacuum interface on the opposite side. The FTS resolution was small enough to barely resolve the fringes. In order for the simulations to match this, they were smoothed using a Gaussian filter to approximate the FTS apodization and resolution.

Table 3. The band-pass peak, resolving power, and transmission of HFSS Sim 1, HFSS Sim 2, HFSS Sim3, and FTS measured performances shown in Fig. 5 *Left* of the room temperature, non-AR coated 44 μm MMBF.

	HFSS Sim 1	HFSS Sim 2	HFSS Sim 3	FTS Measurements
Band-pass Peak Center (THz)	7.0 (43 μm)	7.0 (43 μm)	7.1 (42 μm)	7.1 (42 μm)
$\lambda/\Delta\lambda$	9	10	11	11
Peak Transmission (%)	28	27	26	27

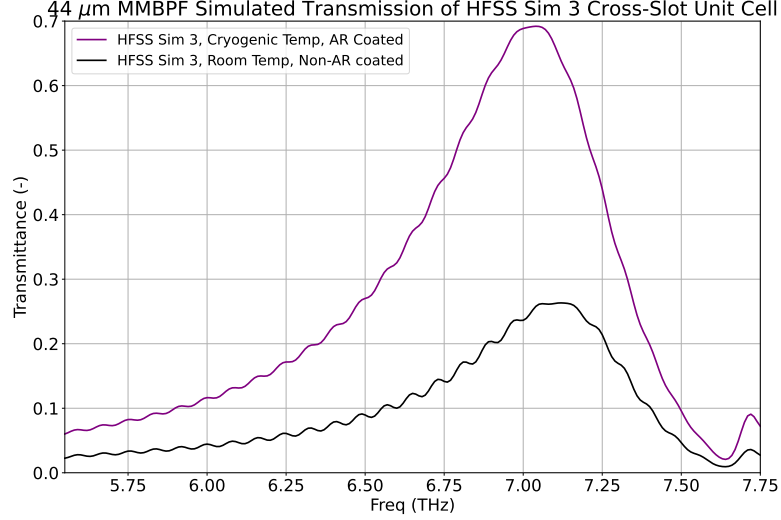


Figure 6. Purple: HFSS simulated transmission of a COC-AR coated cryogenically cooled MMBF with the cross-slot unit cell used in HFSS Sim 3. Bandpass peak = 7.0 THz (43 μm), peak transmission = 69%, and resolving power = 10. Black: HFSS simulated transmission of non-AR coated, room temperature with the cross-slot unit cell used in HFSS Sim 3. The transmission increases by a factor of 2.63 to 69%, due to decreased gold resistive losses at cryogenic temperatures and decreased Si reflective losses from the addition of AR coatings. The second peak at 7.72 THz is due to incident wavelengths less than the periodicity (parameter G in Table 1) of the the mesh grid scattered into higher order modes.⁹ The second peak occurs at the periodicity of the mesh grid ($G = 11.4 \mu\text{m}$), where $7.72 \text{ THz} = 39 \mu\text{m}/\sqrt{\epsilon_r} = 11.4 \mu\text{m}$.

5.2 Transmission-Line Model Fitting

The transmission-line model was fit to HFSS Sim 3 in Fig. 5. The fit has three fit parameters: f_0 the resonant frequency, R and C . L is not a fit parameter because it can be rewritten in terms of C and f_0 , where $L = \frac{1}{\omega_0^2 C}$. A second fit was performed with only two free parameters, f_0 and C . R was fixed to match the DC resistance of the gold film, $0.3 \Omega/\text{sq}$. The fit results are shown in Fig. 7 *Left*. In both fits f_0 is fit well. However, the fringe amplitudes on either side of the bandpass peak are not well fit with our model. This means our model does not fully capture the impedance mismatch at the metal mesh and Si interface. The model is also unable to capture the asymmetry of the filter's transmission profile with the simplified LRC circuit used in Fig. 3. Fig. 7 *Right* compares the smoothed fits to the smoothed HFSS Sim 3 and the FTS measurement. It is clear that the lack of well-fit fringe amplitudes and transmission profile affect the bandwidths in both fits. This leads to bandwidths larger than HFSS Sim 3 and the FTS measurement. The maximum transmission is fit well when R is fixed to $0.3 \Omega/\text{sq}$. When R is a free parameter it is estimated to be $2.75 \times 10^{-1} \Omega/\text{sq}$, which leads to a larger maximum transmission compared to HFSS Sim 3 and the FTS measurement. This further confirms the DC measurement of the gold film and shows that the maximum transmission is mostly dependent on ohmic losses. Table 4, shows the estimated fit parameters. The estimated inductance was calculated from the resonant frequency and capacitance fits. Although the transmission line model does not fully capture the simulation or measurement, it is a useful tool because it enables fast estimation of transmission characteristics as a function of design parameters. We may be able to improve the transmission line model by using a more complex circuit to represent the self-resonant

metal mesh cross-slots.

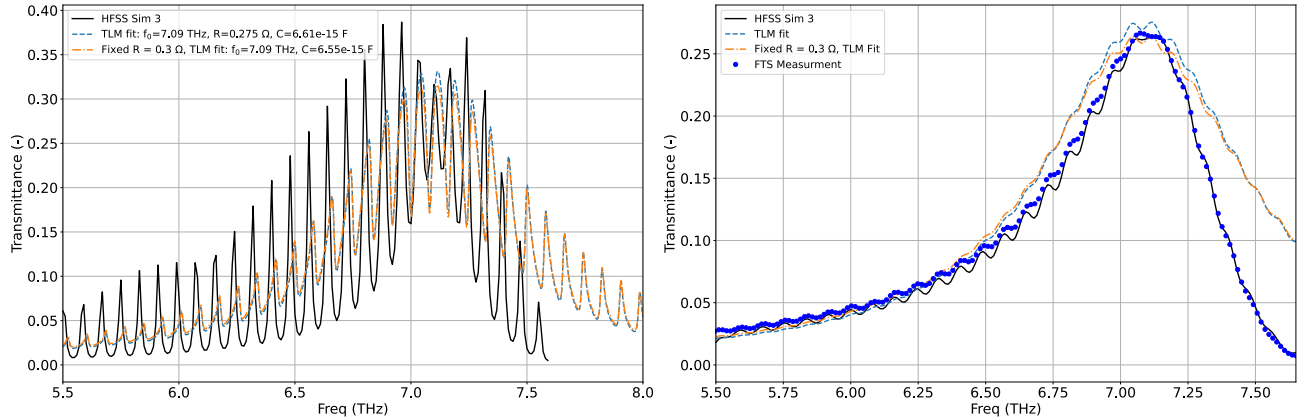


Figure 7. *Left*) Transmission-line model (TLM) fits to HFSS Sim 3 in Fig. 5. Black Line: Simulated transmission of HFSS Sim 3 in Fig. 5. Blue Dashed Line: TLM fit to HFSS Sim 3 with three fit parameters: f_0 , R and C . Orange Dashed-Dotted Line: TLM fit to HFSS Sim 3 with 2 fit parameters: f_0 and C . R was fixed to the measured gold DC resistance of the fabricated $44\ \mu\text{m}$ MMBF, $0.3\ \Omega/\text{sq}$. The fringing along the transmission profile is due to the Si cavity created between the metal mesh and the vacuum interface on the opposite side. *Right*) Smoothed TLM fits in Fig. 7 *Left* compared to smoothed HFSS Sim 3 simulated transmission and the $44\ \mu\text{m}$ MMBF measured transmission (dotted blue line). The lack of well-fit fringe amplitudes and transmission profile shown in Fig. 7 *Left* causes the bandwidths to be larger than HFSS Sim 3 and the FTS measurement.

Table 4. TLM fit parameter values for f_0 , R , C and L . The middle column contains the fit parameters from the blue dashed line in Fig. 7 *Left*. The right column contains the fit parameters from the orange dashed-dotted line in Fig. 7 *Left*, where R was fixed.

	TLM Fit	Fixed R, TLM Fit
f_0 (THz)	7.09	7.09
R (Ω/sq)	0.275	0.300
C (fF)	6.61	6.55
L (fH)	76.2	76.9

6. CONCLUSION AND FUTURE WORK

We have successfully fabricated, measured, and modeled a non-AR coated, room temperature $44\ \mu\text{m}$ MMBF. The transmission at room temperature and non-AR coated was measured to be 27% with a resolving power of 11. When COC-AR coated on both sides the transmission is expected to increase to 69% with a resolving power of 10. The transmission-line model we developed did not fit the simulations well. However, it does help us understand how the maximum transmission changes with resistance and determine how the fringe rate changes with substrate material and thicknesses. We will continue to improve this transmission line model by modifying the circuit used to model the cross-slot resonance.

Our next steps are to characterize cryogenically cooled ($\sim 5\ \text{K}$) COC-AR coated $44\ \mu\text{m}$ filters, LVFs and DVFs. With the simulation methods described and a similar fabrication process, we have begun work to develop LVFs and DVFs for the BEGINS instrument from 25-65 μm and the NFR. Like the $44\ \mu\text{m}$ MMBF, they are made of 100 nm thick gold with cross-slots on a Si substrate. The LVFs and DVFs will have a resolving power of ~ 7 . It should be possible to span the whole wavelength range by scaling the cross-slot parameters, while still preserving the resolving power.^{6,9}

ACKNOWLEDGMENTS

This work is supported by: Future Investigators in NASA Earth and Space Science and Technology (FINESST) grant to Joanna Perido, NASA Astrophysics Research and Analysis (APRA) grant to the California Institute of Technology, JPL, and the University of Colorado-Boulder and a NASA Goddard Space Flight Center Internal Research and Development (IRAD) grant. NFC was supported by an appointment to the NASA Postdoctoral Program at Goddard Space Flight Center, administered by the Oak Ridge Associated Universities under contract with NASA.

REFERENCES

- [1] Glenn, J., Kogut, A., Sharp, E., Cataldo, G., Essinger-Hileman, T., Switzer, E., Denis, K., Rostem, K., Hensley, B., Rosolowsky, E., et al., “Begins: The balloon experiment for galactic infrared science,” in [*American Astronomical Society Meeting Abstracts*], **53**(6), 232–01 (2021).
- [2] National Academies of Sciences, E. and Medicine, [*Origins, Worlds, and Life: A Decadal Strategy for Planetary Science and Astrobiology 2023-2032*], The National Academies Press, Washington, DC (2022).
- [3] Aslam, S., Achterberg, R., Calcutt, S., Cottini, V., Gorius, N., Hewagama, T., Irwin, P., Nixon, C., Quilligan, G., Roos-Serote, M., et al., “Advanced net flux radiometer for the ice giants,” *Space Science Reviews* **216**(1), 1–20 (2020).
- [4] Ulrich, R., “Far-infrared properties of metallic mesh and its complementary structure,” *Infrared Physics* **7**(1), 37–55 (1967).
- [5] Tomaselli, V., Edewaard, D., Gillan, P., and Möller, K., “Far-infrared bandpass filters from cross-shaped grids,” *Applied Optics* **20**(8), 1361–1366 (1981).
- [6] Porterfield, D. W., Hesler, J., Densing, R., Mueller, E., Crowe, T., and Weikle, R., “Resonant metal-mesh bandpass filters for the far infrared,” *Applied Optics* **33**(25), 6046–6052 (1994).
- [7] Möller, K., Warren, J., Heaney, J., and Kotecki, C., “Cross-shaped bandpass filters for the near-and mid-infrared wavelength regions,” *Applied optics* **35**(31), 6210–6215 (1996).
- [8] Melo, A. M., Gobbi, A. L., Piazzetta, M. H., and Da Silva, A. M., “Cross-shaped terahertz metal mesh filters: Historical review and results,” *Advances in Optical Technologies* **2012** (2012).
- [9] Merrell, W. C., Aslam, S., Brown, A. D., Chervenak, J. A., Huang, W.-C., Quijada, M., and Wollack, E. J., “Compact micromachined infrared bandpass filters for planetary spectroscopy,” *Applied optics* **51**(15), 3046–3053 (2012).
- [10] Wollack, E. J., Denis, K. L., Barlis, A., Chang, M.-P., Kuttyrev, A. S., Miller, K. H., and Nagler, P. C., “Far-infrared properties of cyclic olefin copolymer,” *Optics Letters* **45**(3), 780–783 (2020).
- [11] Davis, J., “Bandpass interference filters for very far infrared astronomy,” *Infrared Physics* **20**(4), 287–290 (1980).
- [12] Al-Azzawi, B. F., Rigelsford, J. M., and Langley, R. J., “A systematic transmission line model for the analysis of self-resonant structures within multi-layer dielectric media,” *IEEE Transactions on Microwave Theory and Techniques* **67**(10), 4118–4129 (2019).